metals

MDPI

Article

Molecular Dynamics Investigation on Grain Size-Dependent Superelastic Behavior of CuZr Shape Memory Alloys

Mixun Zhu [1], Kai Wang [1], Hongtao Zhong [1], Huahuai Shen [1], Yong Zhang [2], Xiaoling Fu [1,*] and Yuanzheng Yang [1,*]

[1] School of Materials and Energy, Guangdong University of Technology, Guangzhou 510006, China
[2] Beijing Advanced Innovation Center of Materials Genome Engineering, State Key Laboratory for Advanced Metals and Materials, University of Science and Technology Beijing, 30 Xueyuan Road, Beijing 100083, China; drzhangy@ustb.edu.cn
* Correspondence: fuxiaoling@gdut.edu.cn (X.F.); yangyz@gdut.edu.cn (Y.Y.)

Abstract: The superelasticity of CuZr shape memory alloys (SMAs) originates from stress-induced transformations between the B2 (austenite) and B19′ (martensite) phases. Grain size is a key parameter affecting the superelasticity of shape memory alloys. Previous studies on NiTi, Fe-based, and Cu-based SMAs confirm that altering grain size effectively regulates superelasticity. Current research on the influence of grain size on the superelasticity of CuZr shape memory alloys (SMAs) is relatively sparse. This study employs molecular dynamics simulations to evaluate the effect of grain size on the superelasticity of CuZr SMAs through uniaxial loading–unloading tests. Polycrystalline samples with grain sizes of 6.59 nm, 5 nm, and 4 nm were analyzed. The results indicate that reducing grain size can decrease the irrecoverable strain, thereby enhancing superelasticity. The improvement in superelasticity is attributed to a higher recovery rate of the martensite-to-austenite transformation, allowing more plastic deformation within the grain interior to recover during unloading, and thereby reducing the irrecoverable strain. The recovery rate of the martensite-to-austenite transformation is closely related to the elastic strain energy accumulated within the grain interior during loading.

Keywords: shape memory alloys; superelasticity; grain size effects; irrecoverable strain; phase transformation; molecular dynamics

check for updates

Academic Editor: Gabriel A. Lopez

Received: 31 December 2024
Revised: 27 January 2025
Accepted: 27 January 2025
Published: 29 January 2025

Citation: Zhu, M.; Wang, K.; Zhong, H.; Shen, H.; Zhang, Y.; Fu, X.; Yang, Y. Molecular Dynamics Investigation on Grain Size-Dependent Superelastic Behavior of CuZr Shape Memory Alloys. *Metals* **2025**, *15*, 142. https://doi.org/10.3390/met15020142

Copyright: © 2025 by the authors. Licensee MDPI, Basel, Switzerland. This article is an open access article distributed under the terms and conditions of the Creative Commons Attribution (CC BY) license (https://creativecommons.org/licenses/by/4.0/).

1. Introduction

Shape memory alloys (SMAs) are metallic smart materials that can recover large deformations through the shape memory effect and superelasticity [1]. When a sufficiently large stress is applied to the shape memory alloy, martensite transformation occurs in the specimen, causing a transformation from austenite to martensite and resulting in the plastic deformation of the specimen. When the applied stress is released, the martensitic phase transforms back into the austenitic phase, allowing the specimen to recover its plastic deformation and return to its original shape. The transformation between austenite and martensite under stress is the origin of the superelasticity in shape memory alloys [2–5]. Due to its superelasticity, shape memory alloys such as NiTi, Fe-based, and Cu-based alloys are widely utilized across various fields, including aerospace [6,7], engineering [8–10], and medicine [11]. Compared to the aforementioned shape memory alloys, CuZr shape memory alloys have a lower cost [12], with higher strength, hardness, and better corrosion resistance [13–15]. This means CuZr shape memory alloys can be considered potential replacements for these shape memory alloys in certain applications [16]. Therefore, by

improving the superelasticity of CuZr shape memory alloys, we can further enhance the cost-effectiveness of CuZr shape memory alloys.

Uniaxial loading–unloading is commonly used to test the superelasticity of shape memory alloys. The sample is loaded to a strain (typically 4–8% for NiTi alloys [17,18]) to induce martensite transformation, followed by unloading until the stress reaches 0 GPa. During unloading, as the stress decreases, the martensite phase transforms back to the austenite phase, and a portion of the strain in the shape memory alloy is recovered. After unloading, some strain remains unrecovered, known as irrecoverable strain. In NiTi shape memory alloys, irrecoverable strain arises from plastic deformation at grain boundaries during loading [19,20] and residual martensite within the grain interior after unloading [21,22]. Irrecoverable strain is one of the criteria for evaluating the superelasticity of shape memory alloys [20,23,24]. The smaller the irrecoverable strain, the more superior the superelasticity of the shape memory alloy. The irrecoverable strain of shape memory alloys can be modified by altering the grain size [25]. In the Ti-Nb-Zr system, Zitouni et al. [26] controlled the grain size of samples by adjusting rolling levels, while Kong et al. [27] achieved grain size control by varying annealing durations. Both studies observed that smaller grain sizes resulted in reduced residual strain after loading and unloading, leading to improved superelasticity in the samples. Tseng et al. [28] reported that FeMnAlNi samples with larger grain sizes (>5 mm) had an irrecoverable strain of 1% after unloading under a maximum tensile strain of 3%, while smaller grain sizes (≈2 mm) showed 1.5%. Similarly, Vollmer et al. [29] found that FeMnAlNi samples with a grain size of 7.2 mm exhibited 0.3% irrecoverable strain, while those with a grain size of 2.3 mm showed 0.8% irrecoverable strain during a single loading–unloading cycle. Xu et al. [30] found that NiTi shape memory alloys with an average grain size of 22.29 μm exhibited an irrecoverable strain of 2.7%, while those with 10.59 μm had 0.6% during a single loading–unloading cycle. Liu et al. [21] used molecular dynamics simulations to find that as the grain size decreased from 30 nm to 5 nm, the irrecoverable strain after unloading decreased from 3% to 1% under a maximum tensile strain of 8%.

The main strategy used in recent studies to improve the superelasticity of CuZr shape memory alloys is microalloying, which involves adding elements like Al, Co, and Ni to CuZr shape memory alloys [12,31]. Grain size is a key parameter affecting the superelasticity of shape memory alloys. In NiTi-based, Fe-based, Cu-based, and other shape memory alloys, altering the grain size has been studied and proven to be an effective method for regulating the superelasticity of shape memory alloys. However, there is a lack of research on the effect of grain size on the superelasticity of CuZr shape memory alloys. This study employs molecular dynamics simulations to investigate the effect of grain size on the superelasticity of polycrystalline B2-CuZr samples. By comparing the irrecoverable strain of samples, the effect of grain size within the range of 6.59 nm to 4 nm on the superelasticity is examined. By observing the evolution of local shear strain distribution and the corresponding changes in atomic configuration during the loading and unloading of polycrystalline B2-CuZr samples, the origin of the irrecoverable strain in these samples is analyzed. The volumetric strain within the grain interior and at the grain boundaries of the samples was calculated separately to compare the irrecoverable strain in these regions for polycrystalline B2-CuZr samples with different grain sizes. Furthermore, the factors influencing the irrecoverable strain were analyzed.

2. Modeling and Methods

First of all, three cubes with dimensions of 22.91 nm × 22.91 nm × 22.91 nm were created (Figure 1). The total number of atoms for all three models was approximately 686,000, with the number of Cu and Zr atoms in each model being approximately 343,000.

The polycrystalline structure were generated by utilizing Atomsk software (version Beta 0.13.1) based on the Voronoi construction method [32] to establish three polycrystalline B2-CuZr samples with average grain sizes of 6.59 nm, 5 nm, and 4 nm, respectively (Figure 1). By filling these cubes with varying quantities of grains, we were able to alter the grain sizes of the samples. The number of grains inside the three cubes were 80, 183, and 359, respectively (Table 1). The relationship between the average grain size d_{ave} and number of grains n follows the following formula [33]:

$$d_{ave} = \sqrt[3]{\frac{6V}{\pi n}} \quad (1)$$

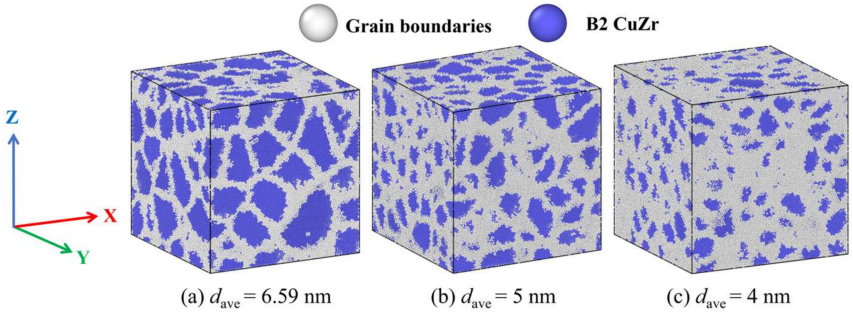


Figure 1. Polycrystalline B2-CuZr samples with different average grain sizes of (**a**) d_{ave} = 6.59 nm, (**b**) d_{ave} = 5 nm, and (**c**) d_{ave} = 4 nm. The B2-CuZr crystals within the grain interior are colored in blue and the grain boundaries are colored in white.

Table 1. The dimension of specimens, grain size, number of grains, number of atoms, and the percentage of grain boundaries and B2 crystalline in the polycrystalline B2-CuZr samples considered in the present molecular dynamics simulations.

The Dimension of Specimens	22.91 nm × 22.91 nm × 22.91 nm		
Grain size (nm)	6.59	5	4
Number of grains	80	183	359
Number of atoms	686,032	685,910	685,942
Grain boundaries (%)	52.0	64.2	75.4
B2 crystallite (%)	48.0	35.8	24.6

Above, V represents the volume of the sample. In this work, we employed the latest embedded atom method (EAM) potential developed by Mendelev et al. [34] and performed molecular dynamics simulations using the open source LAMMPS [35] package. Periodic boundary conditions are applied in all three directions during both the relaxation and loading–unloading stages. The timestep is set to 1 fs. The system was simulated using the isobaric–isothermal (NPT) ensemble under zero external pressure. The temperature and pressure were controlled using a Nosé–Hoover thermostat [36] and a Parrinello–Rahman barostat [37], respectively.

All samples were relaxed for 0.2 ns at 300 K and zero external hydrostatic pressure to relax local atomic structures. Engineering strain is employed as a measure of deformation and denoted by $\varepsilon = (l - l_0)/l_0$, where l is the instantaneous length of the sample and l_0 is its initial length before loading. We performed tensile loading along the X direction of the sample at a strain rate of 10^9 s^{-1} under 300 K and zero external hydrostatic pressure, terminating the loading when the strain reached 0.08. Afterwards, unloading commenced at the same strain rate and was terminated when the stress dropped to 0 GPa. The atomic-scale deformation mechanisms were analyzed using the local shear strain, η_{mises} [38]. We visualized η_{mises} using Open Visualization Tool (OVITO) softwear (version 2.9.0) [39] and

employed polyhedral template matching (PTM) [40] to investigate the phase transformation during the loading and unloading stages of the nanograin structures.

When testing the superelasticity of shape memory alloys, an appropriate maximum tensile strain should be selected to prevent the plastic deformation of martensite within the grain interior, thereby eliminating its influence on the superelastic behavior of the alloy [41]. Based on the combined analysis of the average atomic potential energy and the phase evolution of the crystal, the R phase does not exhibit plastic deformation when the applied tensile strain is less than 0.08 [42]. Therefore, it can be said that a maximum tensile strain of 0.08 is a reasonable strain value for testing the superelasticity of polycrystalline B2-CuZr samples.

In molecular dynamics simulations, the kinetic energy E_k at a given thermodynamic temperature T can be expressed as follows [42]:

$$E_k = \frac{3}{2} N K_b T \tag{2}$$

where K_b is the Boltzmann constant and N is the number of atoms in the system. The total energy of the system is the sum of the kinetic energy and the potential energy. As the average kinetic energy is stable at a constant temperature, the change in potential energy is consistent with the change in total energy. The average potential energy of each atom is quantified and used to describe the phase transition behavior.

3. Results and Discussion

3.1. The Engineering Stress–Strain Curve During Loading and Unloading Process

Figure 2 shows the engineering stress–strain curves of polycrystalline B2-CuZr samples with grain sizes of 6.59 nm, 5 nm, and 4 nm during the loading–unloading process. The sample initially undergoes elastic deformation during loading. As the stress on the sample increases and reaches the critical level for martensitic transformation, the B2 phase begins to transition into the R phase. The critical stress of martensite transformation can be defined as the minimum stress required to initiate the martensite transformation when the sample is subjected to external loading [43]. The corresponding strain to trigger the initiation of the martensitic transformation is the critical strain of martensitic transformation.

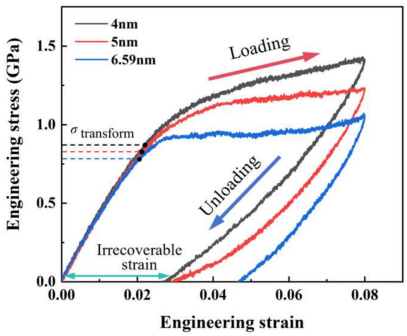


Figure 2. Engineering stress–strain curves of polycrystalline B2-CuZr samples with grain sizes of 6.59 nm, 5 nm, and 4 nm during tensile loading and unloading.

As the grain boundary area consists of a randomized lattice structure without local ordering, and the grain interior is arranged in an ordered structure, the grain boundary phase and the grain interior can often be conceptualized into the crystalline-amorphous composite model. This amorphous-crystalline composite model is often used to describe the shape memory behavior of the B2-NiTi nanocrystalline alloy [44,45]. The grain size effect on the critical stress and strain of martensitic transformation can be explained by the innate interfacial elastic strain model [46]. The innate interfacial elastic strain model

proposes that there is an intrinsic compressive–dilatative elastic strain field when a B2-CuZr crystalline precipitated is embedded into the amorphous matrix. The B2-CuZr crystalline precipitate experiences an intrinsic compressive strain–stress, while the amorphous matrix experiences dilatative strain–stress. As the size of the crystalline precipitate decreases, the compressive strain and stress exerted on the crystalline precipitate by the amorphous matrix increases. The larger the crystalline precipitate is, the smaller the intrinsic compressive strain and stress exerted by the amorphous matrix in the initial state.

During the tensile process of shape memory alloys, when the specimen yields, a martensitic phase transformation occurs. This transformation is reflected on the engineering stress–strain curve as a decrease in slope compared to the elastic deformation stage [47]. Therefore, the critical stress and strain for the martensitic transformation in polycrystalline B2-CuZr samples can be determined by the stress and strain at which the slope of the curve begins to decrease, as shown in Figure 2. For the nanocrystalline specimens in this study, as the average grain sizes decrease from 6.59 nm to 5 nm, and then to 4 nm, the critical stress required to promote martensitic transformation increases from 0.802 GPa to 0.839 GPa and then to 0.901 GPa, and the critical strain needed to induce the structural change from the B2 phase to the R phase increases from 0.0215 to 0.0222 and then to 0.0231, respectively. The increase in the critical stress and strain of martensitic transformation is ascribed to the increase in the compressive stress and strain when the crystalline precipitate embedded in the amorphous phase (the grain boundary phase) becomes smaller [46].

When the applied stress decreases to zero during unloading, the engineering strain of each sample does not completely recover; this non-recoverable strain is commonly referred as irrecoverable strain. When the grain size decreases from 6.59 nm to 5 nm to 4 nm, the irrecoverable strain decreases from 0.046 to 0.030 to 0.026, respectively. This indicates that the irrecoverable strain decreases as the grain size decreases. The nanocrystalline specimen with smaller grain sizes is more capable of reversing the martensite phase back to the austenite phase.

3.2. The Evolution of the Shear Strain Distribution and the Corresponding Phase Configuration During the Loading and Unloading Process

The evolution of the shear strain distribution and the corresponding phase configurations of the three samples with varying grain sizes during loading and unloading are shown in Figure 3. The initial state without applied strain ($\varepsilon = 0$), the critical strain for martensitic transformation, the maximum strain of loading ($\varepsilon = 0.08$), and the end point of unloading were selected for display. As all three specimens display similar trends related to the evolution of the shear strain distribution and the corresponding phase configurations, the samples with an average grain size of 6.59 nm (Figure 3a) were taken as an example. When the tensile strain reaches 0.0215 (critical strain for martensitic transformation), shear strain increases within the grain interior, leading to martensitic transformation which induces the B2 phase to the R phase. The applied tensile strain reaches a maximum value of 0.08 during loading, and the high-shear-strain regions within the grain interior correlate well with the locations of the R phase. A detailed description of the correlation between the high-shear-strain regions within the grain interior and the R phase locations is shown in Figures S1 and S2 of the Supplementary Materials. Additionally, there are regions of high shear strain indicated in red at the grain boundaries. Once the applied strain reaches 0.08, the loading process is terminated. During the unloading process, the shear strain within the grain interior decreases, and some of the martensite R phase reverts back to the initial austenite B2 phase. However, some of the R phase within the grain interior does not have the capability to transfer back to the original B2 phase. These locations still exhibit relatively high shear strain after unloading, indicating that the plastic deformation within the grain interior cannot be fully recovered. For the grain boundary area, no phase transformation

behavior occurs. The shear strain inside the grain boundary area recovers partially, while the unrecovered shear strain suggests that plastic deformation has occurred within the grain boundary area. For samples with average grain sizes of 5 nm (Figure 3b) and 4 nm (Figure 3c), they display similar trends to the specimen with average grain sizes of 6.59 nm. Therefore, the irrecoverable shear strain may come from two sources: the first one is the irrecoverable strain related to the un-reverted phase transformation, and the other one is ascribed to the plastic deformation of the grain boundary area.

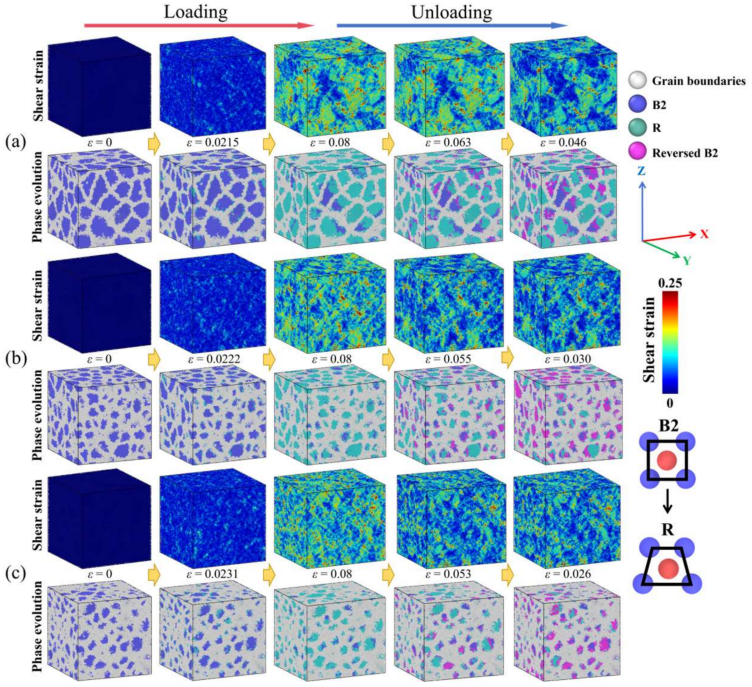


Figure 3. The evolution of local shear strain distribution and the corresponding phase configuration in polycrystalline B2-CuZr samples with grain sizes of (**a**) 6.59 nm, (**b**) 5 nm, and (**c**) 4 nm. The initial state without applied strain ($\varepsilon = 0$), the critical strain for martensitic transformation, the maximum strain of loading ($\varepsilon = 0.08$), and the end point of unloading were selected for display.

Figure 4 presents the process of phase evolution (including the grain boundary, the B2 phase, and the R phase) during loading and unloading. We take the nanocrystalline specimen with an average grain size of 6.59 nm as an example (Figure 4a). Before loading, the percentages of the grain boundary phase, the B2 phase, and the R phase are 52.0%, 48.0%, and 0%, respectively. With increasing strain, the percentage of the B2 phase and the R phase shows negligible change. As the strain reaches 0.0215, the B2 phase begins to transform into the R phase. A proportion of the B2 phase gradually decreases to 9.2% when the tensile strain reaches the maximum value of 0.08. The fraction of the R phase reaches a maximum value of 38.7%. During the unloading process, as the tensile strain gradually decreases from 0.08 to 0.046, some of the R phase reverts back to the B2 phase, resulting in an increase in the B2 phase and a decrease in the R phase. The amount of grain boundary phase remains unchanged throughout the entire loading–unloading process.

For nanocrystalline specimens with average grain sizes of 5 nm and 4 nm, the evolution of the phase components is similar to that of the specimen with an average grain size of 6.59 nm (Figure 4b,c). Table 2 summarizes the proportions of all phases during the loading–unloading processes. There are some similarities and differences that are worth noting: (1) The transformation rate from the B2 phase to the R phase is 80.8%, 80.4%, and 80.9% for specimens with average grain sizes of 6.59 nm, 5 nm, and 4 nm, respectively. This means the grain size does not significantly impact the transformation rate from the austenite B2 phase to the martensite R phase during loading. (2) The recoverable rate from the

martensite R phase to the B2 phase is 32.0%, 70.1%, and 78.9 for specimens with average grain sizes of 6.59 nm, 5 nm, and 4 nm, respectively. It appears that the recovery rate of the R phase increases as the grain size decreases. What is noteworthy is that when the grain size is smaller than 5 nm, the recoverable rate of the R phase to the B2 phase can be quite high, exceeding 70%. However, once the grain size exceeds 6.59 nm, the recoverable rate significantly decreases to 32.0%. Although the increase in the grain size is less than 2 nm, the recovery rate decreases substantially by more than 38%. Additionally, the plastic deformation of the specimen at a tensile strain of 8% can be obtained by subtracting the elastic strain during loading from the maximum tensile strain of 8%, as shown in Table 2. As the grain size decreases from 6.59 nm to 5 nm to 4 nm, the elastic strain during loading increases from 2.15% to 2.22% to 2.31%, while the plastic strain at the maximum tensile strain decreases from 5.85% to 5.78% to 5.69%, respectively.

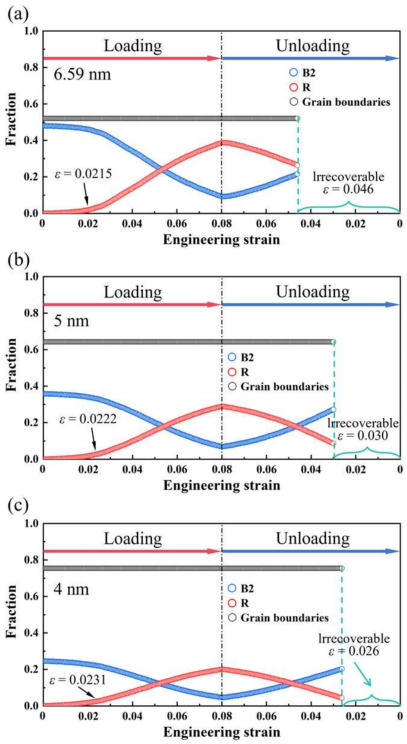


Figure 4. Phase content evolution of polycrystalline B2-CuZr samples with grain sizes of (**a**) 6.59 nm, (**b**) 5 nm, and (**c**) 4 nm during loading and unloading.

Table 2. The phase proportions of polycrystalline B2-CuZr samples with different grain sizes during the loading–unloading processes, including the transformation rate of the B2 phase after loading and the recovery rate of the R phase after unloading. The elastic and plastic strains of the samples during the loading process were also evaluated.

Grain size (nm)	6.59	5	4
Grain boundaries (%)	52.0	64.2	75.4
Elastic strain during loading (%)	2.15	2.22	2.31
B2 phase before loading, ε = 0 (%)	48.0	35.8	24.6
B2 phase after loading, ε = 8% (%)	9.2	7.0	4.7
B2 phase after unloading (%)	21.7	27.2	20.4
Transformation rate of B2 phase during loading (%)	80.8	80.4	80.9

Table 2. *Cont.*

R phase before loading, ε = 0 (%)	0	0	0
R phase after loading, ε = 8% (%)	38.7	28.8	19.9
R phase after unloading (%)	26.3	8.6	4.2
Recovery rate of R phase during unloading (%)	32.0	70.1	78.9
Irrecoverable rate of R phase during unloading (%)	68.0	29.9	21.1
Plastic strain at maximum tensile strain 8% (%)	5.85	5.78	5.69

3.3. The Correlation Between the Irrecoverable Strain and the Average Atomic Volume

To further understand how much of the irrecoverable strain comes from the irrecoverable strain induced by un-reverted phase transformation behavior, and how much of the irrecoverable strain comes from the plastic deformation of the grain boundary area, the volumetric strain ε_V was used to calculate the irrecoverable strain. The grains in polycrystalline materials are randomly oriented, allowing polycrystalline materials to be considered isotropic [48]. For isotropic materials, the relationship between volumetric strain and linear strain is as follows [49]:

$$\varepsilon_V \approx (1 - 2v)\varepsilon_l \tag{3}$$

In Equation (1), v represents the Poisson's ratio of the sample. ε_l represents the linear strain in the loading direction, referring to the irrecoverable strain of the sample. ε_V represents the volumetric strain of the sample. The formula for calculating the volumetric strain ε_V is given by the following:

$$\varepsilon_V = \frac{\overline{V}_{\text{after loading}} - \overline{V}_{\text{before loading}}}{\overline{V}_{\text{before loading}}} \times 100\% \tag{4}$$

In Equation (2), $\overline{V}_{\text{before loading}}$ is the average atomic volume of the sample before loading, and $\overline{V}_{\text{after unloading}}$ is the average atomic volume of the sample after the loading–unloading process. The average atomic volume refers to the mean volume of the Voronoi cell corresponding to each atom in a polycrystalline B2-CuZr sample. It is obtained by calculating the Voronoi cell volume for each atom in the sample and then taking the average of these values. The results are shown in Figure 5a. When the grain size decreases from 6.59 nm to 5 nm to 4 nm, the volumetric strain of the samples decreases from 0.82% to 0.30% to 0.16%, while the irrecoverable strain of samples decreases from 0.046 to 0.030 to 0.026, respectively. This indicates that the smaller the volumetric strain of the samples, the smaller the irrecoverable strain. We calculated the volumetric strain within the grain interiors and grain boundaries of polycrystalline B2-CuZr samples with different grain sizes, and the results are shown in Figure 5b. When the grain size decreases from 6.59 nm to 5 nm to 4 nm, the volumetric strain within the grain interior decreases from 0.52% to 0.20% to 0.11%, respectively, while the volumetric strain at the grain boundaries decreases from 0.30% to 0.10% to 0.05%. From Equation (3), the volumetric strain can be associated with the irrecoverable strain in a linear relationship. The decrease in the volumetric strain is linked to the decrease in the irrecoverable strain. We can therefore infer that the irrecoverable strain within the grain interior and at the grain boundaries decreases as the grain size decreases. From Figure 5b, the volumetric strain of the grain interior is much higher than that of the grain boundary for all three specimens, indicating that the irrecoverable strain within the grain interior plays a more significant role than that at the grain boundaries.

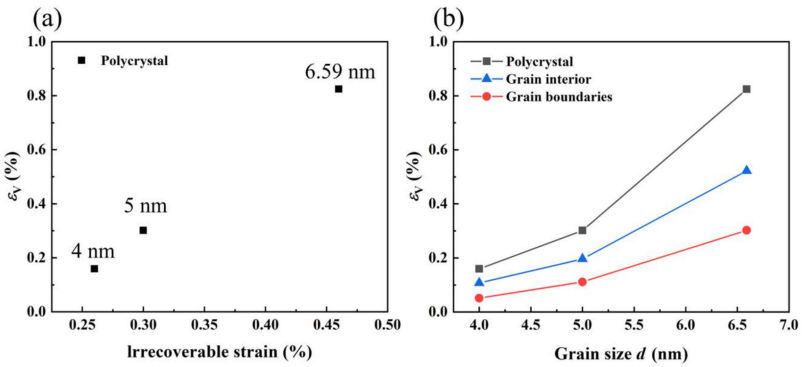


Figure 5. (**a**) The volumetric strain ε_V and irrecoverable strain of polycrystalline B2-CuZr samples with different grain sizes. (**b**) The volumetric strain ε_V of polycrystal, grain interior, and grain boundaries with different grain sizes.

As the irrecoverable strain comes from two factors, one is from lattice rearrangement induced by the uncoverable phase within the grain interior; another is from the plastic deformation at the grain boundary area. The following will discuss the grain size effect on the irrecoverable strain from within the grain interior and along the grain boundaries, respectively.

3.4. The Potential Energy Evolution During the Reversion Process of the Martensitic Transformation from the Grain Interior and the Grain Boundary Phase

When the austenite phase transforms into the martensite phase, both the shape and volume of the lattice structure change. As the change in shape and volume are constrained by the grain boundary phase, elastic strain energy is stored within the grain interior [25,50,51]. The stability of the martensite phase will be affected by the strain energy [52]. The higher the stored strain energy, the lower the stability of the martensite phase. The recovery rate of the strained martensite phase will be higher.

Strain energy is a type of potential energy stored within a material when it is deformed elastically. The material can regain its original shape after the applied force is removed. As the irrecoverable strain comes from both within the grain interior and the grain boundary phase, the potential energies of the nanocrystalline specimens, the grain interior, and the grain boundary phase were extracted to evaluate the effect of stored energy from different lattice structures on superelasticity.

External loading usually increases the potential energy [42], while phase transformation behavior alone tends to decrease the potential energy [46]. The trend of potential energy during loading–unloading is presented along with the Engineering stress–strain curve in Figure 6. The potential energies for the polycrystal, the grain boundary phase, and the grain interior were calculated separately to understand the effect of superelasticity on the grain interior and the grain boundary phase. Figure 6a presents the nanocrystalline specimen with an average grain size of 6.59 nm. From point O_I to A_I, both the grain boundary and the grain interior experiences elastic deformation, and the potential energy increases. The elastic strain is recoverable from the O_I to A_I stage. From A_I to B_I, the grain interior experiences phase transformation from the B2 structure to the R structure (Figure 3a—phase evolution). Part of the grain boundary continues to deform elastically, and part of the grain boundary experiences plastic deformation. The elastic deformation increases the potential energy and the plastic deformation decreases the potential energy [53]. In Figure 6a, the grain boundary potential energy increases, indicating that the deformation of the grain boundary is predominantly elastic. The higher plastic deformation regime along the grain boundary area is shown in red in Figure 3a—shear strain.

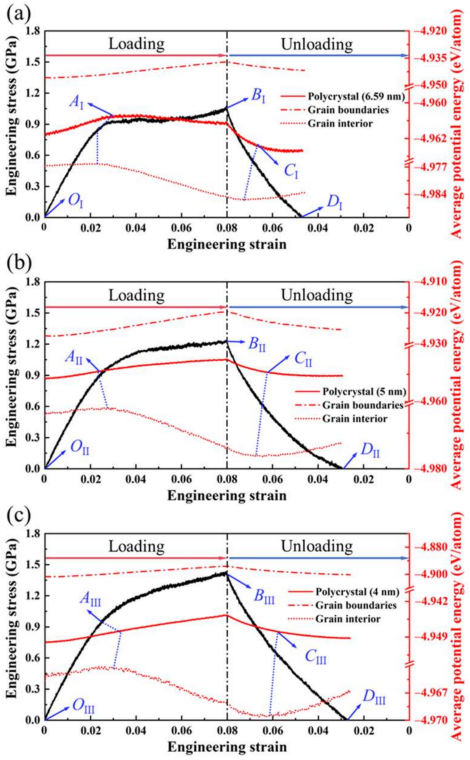


Figure 6. The engineering stress–strain curves of polycrystalline B2-CuZr samples with grain sizes of (**a**) 6.59 nm, (**b**) 5 nm, and (**c**) 4 nm and the corresponding potential energy changes with applied strain.

At point B_I, the tensile strain reaches 0.08, and the unloading process subsequently starts at a strain rate of 10^9 s^{-1}. During unloading, the removal of the external force will decrease the potential energy, while the release of the elastic strain energy during the reversion process of the martensite phase to the austenite lattice structure will help increase the potential energy [19]. During the unloading process from B_I to D_I (ε = 0.046), 32.0% of the martensite R phase reverts back to the austenite B2 phase, and the remaining 68.0% of the martensite R phase is not capable of reverting back to the R phase. The potential energy of the grain interior decreases initially, followed by an increase. From B_I to C_I, the decreasing trend in the potential energy within the grain interior is primarily governed by the removal of the external force. From C_I to D_I, the increasing trend is mainly controlled by the reversal process of phase transformation. From B_I to C_I to D_I, the evolution of the potential energy in the grain boundary phase during unloading is mainly dominated by the removal of the external force. The evolution of the potential energy in the polycrystalline is just the combination of the potential energy evolution in the grain boundary phase and the grain interior.

For the nanocrystalline specimens with average grain sizes of 5 nm and 4 nm, the evolution of the potential energy follows a similar trend (Figure 6b,c).

3.5. The Correlation Between the Elastic Strain Energy Within the Grain Interior and the Recovery Rate of R Phase During Unloading

During the loading process, the changes in shape and volume resulting from phase transformation were constrained by the grain interior (crystalline)–grain (amorphous) boundary. The transformation strain was accumulated within the grain interior. During the unloading process, within the grain interior, some regions experienced phase transformations, while some regions experienced high elastic strain. These atoms with higher elastic strain would tend to release the potential energy to become more stable. Therefore, the

higher the elastic energy within the grain interior, the greater the driving force with which the martensite R phase transforms back into the austenite B2 phase.

The elastic energy accumulated during loading (from *O* to *B* in Figure 6) within the grain interior was calculated and is presented in Figure 7. As the grain size decreases from 6.59 nm to 5 nm, and then to 4 nm, the average elastic strain energy per atom decreases from 0.18 eV/atom to 0.16 eV/atom, and subsequently to 0.11 eV/atom, respectively. It appears there is a linear correlation between the decrease in average elastic strain energy per atom within the grain interior and the decrease in the average grain size. As the grain size decreases from 6.59 nm to 5 nm to 4 nm, the recovery rate of the R phase to the B2 phase during unloading increases from 32.0% to 70.1 to 78.9%, respectively. There is a strong correlation between the recovery rate of the martensite R phase and the elastic strain energy within the grain interior.

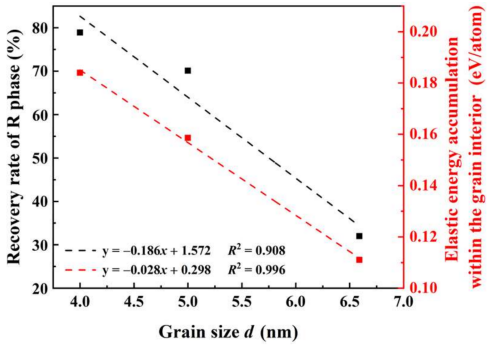


Figure 7. The correlation between the recovery rate of the R phase and the elastic energy accumulation within the grain interior during loading.

4. Conclusions

The grain size effect on the superelasticity of the B2-CuZr nanocrystalline were studied through molecular dynamics simulation. For polycrystalline samples with grain sizes ranging from 4 nm to 6.59 nm, particularly those with grain boundary percentages between 52% and 75.4%, or grain interior percentages between 24.6% and 48%, the major conclusions can be drawn as follows:

(1) The smaller the grain size, the higher the recovery rate of the martensite-to-austenite transformation, and the better the superelasticity.
(2) The critical strain and stress of martensitic transformation during loading can be well explained by the "innate interfacial elastic strain model", which consists of a B2 crystalline precipitate embedded in an amorphous matrix.
(3) The recovery rate of the martensite-to-austenite transformation is closely correlated with the elastic strain energy within the grain interior accumulated during the austenite-to-martensite process while loading.

Supplementary Materials: The following supporting information can be downloaded at https://www.mdpi.com/article/10.3390/met15020142/s1, Figure S1. The shear strain and phase configuration of the polycrystalline B2-CuZr sample with a grain size of 6.59 nm at the critical strain for martensitic transformation (ε = 0.0215); Figure S2. The shear strain and phase configuration of the polycrystalline B2-CuZr sample with a grain size of 6.59 nm at the maximum tensile strain (ε = 0.08).

Author Contributions: Conceptualization, X.F. and M.Z.; methodology, X.F. and M.Z.; software, H.Z. and H.S.; validation, K.W., Y.Z. and Y.Y.; formal analysis, K.W., H.Z. and H.S.; investigation, M.Z., H.Z. and H.S.; resources, X.F. and Y.Y.; data curation, M.Z.; writing—original draft preparation, M.Z.; writing—review and editing, M.Z. and X.F.; visualization, Y.Z., H.S. and Y.Y.; supervision, X.F.; project

administration, X.F.; funding acquisition, X.F. All authors have read and agreed to the published version of the manuscript.

Funding: This research was funded by the National Natural Science Foundation of China (Grant No. 52471005, 52071089); the Guangdong Major Project of Basic and Applied Basic Research (Grant No. 2019B030302010); and the Guangdong Basic and Applied Basic Research Foundation (Grant No. 2022A1515010233, 2024A1515010878). This work was supported by open research fund No. 2020-Z11 from the State Key Laboratory for Advanced Metals and Materials, University of Science and Technology, Beijing, China.

Data Availability Statement: The original contributions presented in this study are included in the article/supplementary material. Further inquiries can be directed to the corresponding authors.

Conflicts of Interest: The authors declare that they have no known competing financial interests or personal relationships that could have appeared to influence the work reported in this paper.

References

1. Saedi, S.; Acar, E.; Raji, H.; Saghaian, S.E.; Mirsayar, M. Energy damping in shape memory alloys: A review. *J. Alloys Compd.* **2023**, *956*, 170286. [CrossRef]
2. Koval, Y.N.; Firstov, G.S.; Kotko, A.V. Martensitic transformation and shape memory effect in ZrCu intermetallic compound. *Scr. Metall. Mater.* **1992**, *27*, 1611–1616. [CrossRef]
3. Šittner, P.; Iaparova, E.; Molnárová, O.; Tyc, O.; Bian, X.; Kadeřávek, L.; Heller, L. Recoverable and plastic strains generated by forward and reverse martensitic transformations under external stress in NiTi SMA wires. *Mater. Des.* **2024**, *244*, 113188. [CrossRef]
4. Huang, Y.; Dong, J.; Yang, M.; Zhang, Y.; Lu, Z.; Wei, X.; Zhao, J.; Song, W.; Liu, X.; Wang, H.; et al. Frictional shear stress-induced incomplete martensitic transformation in mono-crystalline B2-CuZr spherulites. *Acta Mater.* **2024**, *267*, 119705. [CrossRef]
5. Jaydeepkumar Oza, M.; Stark, A.; Polatidis, E.; Barriobero Vila, P.; Shahverdi, M.; Leinenbach, C. Characterization of low-temperature creep and stress relaxation of an iron-based shape memory alloy (Fe-SMA) using in-situ synchrotron diffraction. *Mater. Des.* **2024**, *247*, 113378. [CrossRef]
6. Lau, K.T.; Ling, H.Y.; Zhou, L.M. Low velocity impact on shape memory alloy stitched composite plates. *Smart Mater. Struct.* **2004**, *13*, 364. [CrossRef]
7. Tsoi, K.A.; Stalmans, R.; Schrooten, J.; Wevers, M.; Mai, Y.-W. Impact damage behaviour of shape memory alloy composites. *Mater. Sci. Eng. A* **2003**, *342*, 207–215. [CrossRef]
8. Kwon, S.-C.; Jo, M.-S.; Oh, H.-U. Experimental Validation of Fly-Wheel Passive Launch and On-Orbit Vibration Isolation System by Using a Superelastic SMA Mesh Washer Isolator. *Int. J. Aerosp. Eng.* **2017**, *2017*, 5496053. [CrossRef]
9. Alaneme, K.K.; Okotete, E.A.; Anaele, J.U. Structural vibration mitigation—A concise review of the capabilities and applications of Cu and Fe based shape memory alloys in civil structures. *J. Build. Eng.* **2019**, *22*, 22–32. [CrossRef]
10. Shukla, U.; Garg, K. Journey of smart material from composite to shape memory alloy (SMA), characterization and their applications—A review. *Smart Mater. Med.* **2023**, *4*, 227–242. [CrossRef]
11. Wang, Y.; Venezuela, J.; Dargusch, M. Biodegradable shape memory alloys: Progress and prospects. *Biomaterials* **2021**, *279*, 121215. [CrossRef] [PubMed]
12. De Luca, F.; Nnamchi, P.; Younes, A.; Fry, A.T.; González, S. Stress-induced martensitic transformation of Cu50Zr50 shape memory alloy optimized through microalloying and co-microalloying. *J. Alloys Compd.* **2019**, *781*, 337–343. [CrossRef]
13. Song, K.K.; Han, X.L.; Pauly, S.; Qin, Y.S.; Kosiba, K.; Peng, C.X.; Gong, J.H.; Chen, P.X.; Wang, L.; Sarac, B.; et al. Rapid and partial crystallization to design ductile CuZr-based bulk metallic glass composites. *Mater. Des.* **2018**, *139*, 132–140. [CrossRef]
14. Zheng, J.; Miao, Y.; Zhang, H.; Chen, S.; Lee, D.; Arróyave, R.; Vlassak, J.J. Phase transformations in equiatomic CuZr shape memory thin films analyzed by differential nanocalorimetry. *Acta Mater.* **2018**, *159*, 320–331. [CrossRef]
15. He, C.; Zhang, M.; Zhang, W.X. Electronic structure and generalized stacking fault energy of CuZr-X (X=Al, Fe, Ni and Zn) intermetallic compounds by first-principles calculations. *Solid State Commun.* **2019**, *303–304*, 113736. [CrossRef]
16. Younes, A.; Izadi-Gonabadi, H.; Sánchez, R.M.; Bull, S.J.; González, S. Unravelling the combined effect of cooling rate and microalloying on the microstructure and tribological performance of Cu50Zr50. *Wear* **2022**, *494–495*, 204276. [CrossRef]
17. Kabirifar, P.; Chu, K.; Ren, F.; Sun, Q. Effects of grain size on compressive behavior of NiTi polycrystalline superelastic macro- and micropillars. *Mater. Lett.* **2018**, *214*, 53–55. [CrossRef]
18. Ahadi, A.; Sun, Q. Effects of grain size on the rate-dependent thermomechanical responses of nanostructured superelastic NiTi. *Acta Mater.* **2014**, *76*, 186–197. [CrossRef]

19. Nie, K.; Li, M.-P.; Wu, W.-P.; Sun, Q.-P. Grain size-dependent energy partition in phase transition of NiTi shape memory alloys studied by molecular dynamics simulation. *Int. J. Solids Struct.* **2021**, *221*, 31–41. [CrossRef]
20. Wang, M.; Jiang, S.; Zhang, Y.; Sun, D.; Yan, B. Molecular dynamics investigation on mechanical behaviour and phase transition of nanocrystalline NiTi shape memory alloy containing amorphous surface. *Appl. Surf. Sci.* **2022**, *587*, 152871. [CrossRef]
21. Liu, B.; Li, Z.; Du, C.; Wu, W. Molecular dynamics simulation of grain size effect on mechanism of twin martensite transformation of nanocrystalline NiTi shape memory alloys. *Comput. Mater. Sci.* **2022**, *210*, 111451. [CrossRef]
22. Ko, W.-S.; Choi, W.; Xu, G.-K.; Choi, P.P.; Ikeda, Y.; Grabowski, B. Dissecting functional degradation in NiTi shape memory alloys containing amorphous regions via atomistic simulations. *Acta Mater.* **2021**, *202*, 331–349. [CrossRef]
23. Yan, A.; Cai, W.S.; Li, H.Z.; Lu, H.Z.; Lin, J.M.; Wang, J.; Zhang, L.C.; Yang, C. Stable superelasticity with large recoverable strain in NiTi alloy via additive manufacturing. *Mater. Sci. Eng. A* **2024**, *911*, 146935. [CrossRef]
24. Jin, X.; Li, J.; Yang, J.; Wang, X.; Na, S.; Zhang, M.; Xu, H.; Tian, X.; Zhao, W.; Zhang, H.; et al. Superelasticity with narrow stress hysteresis and high cyclic stability in Co–V–Al polycrystalline alloy. *J. Mater. Res. Technol.* **2024**, *32*, 77–85. [CrossRef]
25. Ko, W.-S.; Maisel, S.B.; Grabowski, B.; Jeon, J.B.; Neugebauer, J. Atomic scale processes of phase transformations in nanocrystalline NiTi shape-memory alloys. *Acta Mater.* **2017**, *123*, 90–101. [CrossRef]
26. Zitouni, I.; Abuzaid, W.; Egilmez, M.; Alkhader, M. Experimental assessment of the functional fatigue in biocompatible Ti67Zr19Nb11.5Sn2.5 shape memory alloy in the vicinity of drilled holes. *J. Mater. Res. Technol.* **2023**, *27*, 3016–3028. [CrossRef]
27. Kong, L.; Wang, B.; Sun, S.; Hang, X.; Meng, X.; Zheng, Y.; Gao, Z. Microstructure, superelasticity and elastocaloric behavior of Ti-18Zr-11 Nb-3Sn strain glass alloys by thermomechanical treatment. *J. Alloys Compd.* **2022**, *905*, 164237. [CrossRef]
28. Tseng, L.W.; Ma, J.; Vollmer, M.; Krooß, P.; Niendorf, T.; Karaman, I. Effect of grain size on the superelastic response of a FeMnAlNi polycrystalline shape memory alloy. *Scr. Mater.* **2016**, *125*, 68–72. [CrossRef]
29. Vollmer, M.; Arold, T.; Kriegel, M.J.; Klemm, V.; Degener, S.; Freudenberger, J.; Niendorf, T. Promoting abnormal grain growth in Fe-based shape memory alloys through compositional adjustments. *Nat. Commun.* **2019**, *10*, 2337. [CrossRef]
30. Xu, K.; Luo, J.; Li, C.; Shen, Y.; Li, C.; Ma, X.; Li, M. Mechanisms of stress-induced martensitic transformation and transformation-induced plasticity in NiTi shape memory alloy related to superelastic stability. *Scr. Mater.* **2022**, *217*, 114775. [CrossRef]
31. Biffi, C.A.; Fiocchi, J.; Coduri, M.; Tuissi, A. Effect of Al Addition on Martensitic Transformation Stability and Microstructural and Mechanical Properties of CuZr Based Shape Memory Alloys. *Metals* **2021**, *11*, 1141. [CrossRef]
32. Hirel, P. Atomsk: A tool for manipulating and converting atomic data files. *Comput. Phys. Commun.* **2015**, *197*, 212–219. [CrossRef]
33. Li, J.; Lu, B.; Zhang, Y.; Zhou, H.; Hu, G.; Xia, R. Nanoindentation response of nanocrystalline copper via molecular dynamics: Grain-size effect. *Mater. Chem. Phys.* **2020**, *241*, 122391. [CrossRef]
34. Mendelev, M.I.; Sun, Y.; Zhang, F.; Wang, C.Z.; Ho, K.M. Development of a semi-empirical potential suitable for molecular dynamics simulation of vitrification in Cu-Zr alloys. *J. Chem. Phys.* **2019**, *151*, 214502. [CrossRef]
35. Plimpton, S. Fast Parallel Algorithms for Short-Range Molecular Dynamics. *J. Comput. Phys.* **1995**, *117*, 1–19. [CrossRef]
36. Nosé, S. A unified formulation of the constant temperature molecular dynamics methods. *J. Chem. Phys.* **1984**, *81*, 511–519. [CrossRef]
37. Parrinello, M.; Rahman, A. Polymorphic transitions in single crystals: A new molecular dynamics method. *J. Appl. Phys.* **1981**, *52*, 7182–7190. [CrossRef]
38. Shimizu, F.; Ogata, S.; Li, J. Theory of Shear Banding in Metallic Glasses and Molecular Dynamics Calculations. *Mater. Trans.* **2007**, *48*, 2923–2927. [CrossRef]
39. Stukowski, A. Visualization and Analysis of Atomistic Simulation Data with OVITO—The Open Visualization Tool. *Model. Simul. Mater. Sci. Eng.* **2010**, *18*, 015012. [CrossRef]
40. Larsen, P.M.; Schmidt, S.; Schiøtz, J. Robust structural identification via polyhedral template matching. *Model. Simul. Mater. Sci. Eng.* **2016**, *24*, 055007. [CrossRef]
41. Wang, M.; Jiang, S.; Sun, D.; Zhang, Y. Orientation dependence of mechanical behavior and phase transformation of NiTi shape memory alloy with multilayer structures by molecular dynamics simulation. *J. Mater. Res. Technol.* **2022**, *18*, 943–961. [CrossRef]
42. Wu, J.; Zhu, M.; Li, S.; Zhong, H.; Li, P.; Song, K.; Song, W.; Tan, M.J.; Yang, Y.; Fu, X. Different phase transformation behaviors of B2-CuZr crystalline phase and their associated mechanical properties by molecular dynamics using different potentials. *Mater. Today Commun.* **2024**, *40*, 109474. [CrossRef]
43. Sidharth, R.; Mohammed, A.S.K.; Abuzaid, W.; Sehitoglu, H. Unraveling Frequency Effects in Shape Memory Alloys: NiTi and FeMnAlNi. *Shape Mem. Superelasticity* **2021**, *7*, 235–249. [CrossRef]
44. Li, M.P.; Sun, Q.P. Nanoscale phase transition behavior of shape memory alloys—Closed form solution of 1D effective modelling. *J. Mech. Phys. Solids* **2018**, *110*, 21–37. [CrossRef]
45. Zhang, Y.; Jiang, S.; Lin, P.; Yang, L. Physical mechanisms for dependence of temperature-induced phase transition and shape memory effect on grain size in nanocrystalline NiTi shape memory alloys. *J. Alloys Compd.* **2024**, *1002*, 175225. [CrossRef]
46. Fu, X.; Lin, Y.; Zhu, M.; Wang, K.; Wu, J.; Tong, X.; Song, W.; Tan, M.J.; Yang, Y.; Shen, J.; et al. The innate interfacial elastic strain field of a transformable B2 precipitate embedded in an amorphous matrix. *npj Comput. Mater.* **2023**, *9*, 226. [CrossRef]

47. Fan, M.; Guo, H.; Li, S.; Han, Y.; Pan, Y. Experimental and numerical study on the mechanical properties of NiTi-SMA bars. *Structures* **2023**, *58*, 105425. [CrossRef]
48. Wang, V.; Xu, N.; Liu, J.-C.; Tang, G.; Geng, W.-T. VASPKIT: A user-friendly interface facilitating high-throughput computing and analysis using VASP code. *Comput. Phys. Commun.* **2021**, *267*, 108033. [CrossRef]
49. Megson, T.H.G. Chapter 7—Stress and Strain. In *Structural and Stress Analysis*, 3rd ed.; Megson, T.H.G., Ed.; Butterworth-Heinemann: Boston, MA, USA, 2014; pp. 146–183.
50. Nakada, N.; Ishibashi, Y.; Tsuchiyama, T.; Takaki, S. Self-stabilization of untransformed austenite by hydrostatic pressure via martensitic transformation. *Acta Mater.* **2016**, *110*, 95–102. [CrossRef]
51. Ahadi, A.; Sun, Q. Stress-induced nanoscale phase transition in superelastic NiTi by in situ X-ray diffraction. *Acta Mater.* **2015**, *90*, 272–281. [CrossRef]
52. Waitz, T.; Antretter, T.; Fischer, F.D.; Karnthaler, H.P. Size effects on martensitic phase transformations in nanocrystalline NiTi shape memory alloys. *Mater. Sci. Technol.* **2008**, *24*, 934–940. [CrossRef]
53. Li, S.; Wu, J.; Chen, X.; Zhu, M.; Chen, J.; Xue, P.; Huang, Y.; Tan, M.J.; Yang, Y.; Fu, X. Two-stage work-hardening of a transformable B2-enhanced metallic glass composite by molecular dynamics simulation. *Compos. Commun.* **2024**, *51*, 102045. [CrossRef]

Disclaimer/Publisher's Note: The statements, opinions and data contained in all publications are solely those of the individual author(s) and contributor(s) and not of MDPI and/or the editor(s). MDPI and/or the editor(s) disclaim responsibility for any injury to people or property resulting from any ideas, methods, instructions or products referred to in the content.